

# Electron and hole doping in the relativistic Mott insulator $\text{Sr}_2\text{IrO}_4$ : A first-principles study using band unfolding technique

Peitao Liu,<sup>1,2</sup> Michele Reticcioli,<sup>1</sup> Bongjae Kim,<sup>1</sup> Alessandra Continenza,<sup>3</sup> Georg Kresse,<sup>4</sup> D. D. Sarma,<sup>5</sup>  
Xing-Qiu Chen,<sup>2</sup> and Cesare Franchini<sup>1,\*</sup>

<sup>1</sup>University of Vienna, Faculty of Physics and Center for Computational Materials Science, Sensengasse 8/8, A-1090 Vienna, Austria

<sup>2</sup>Shenyang National Laboratory for Materials Science, Institute of Metal Research, Chinese Academy of Sciences, Shenyang 110016, China

<sup>3</sup>Department of Information Engineering, Computer Science and Mathematics, University of L'Aquila, Via Vetoio, 67100 Coppito (AQ), Italy

<sup>4</sup>University of Vienna, Faculty of Physics and Center for Computational Materials Science, Sensengasse 8/12, A-1090 Vienna, Austria

<sup>5</sup>Solid State and Structural Chemistry Unit, Indian Institute of Science, Bangalore-560012, India

(Received 28 June 2016; revised manuscript received 9 November 2016; published 28 November 2016)

We study the effects of dilute La and Rh substitutional doping on the electronic structure of the relativistic Mott insulator  $\text{Sr}_2\text{IrO}_4$  using fully relativistic and magnetically noncollinear density functional theory with the inclusion of an on-site Hubbard  $U$ . To model doping effects, we have adopted the supercell approach, that allows for a realistic treatment of structural relaxations and electronic effects beyond a purely rigid band approach. By means of the band unfolding technique we have computed the spectral function and constructed the effective band structure and Fermi surface (FS) in the primitive cell, which are readily comparable with available experimental data. Our calculations clearly indicate that La and Rh doping can be interpreted as effective electron and (fractional) hole doping, respectively. We found that both electron and hole doping induce an insulating-to-metal transition (IMT) but with different characteristics. In  $\text{Sr}_{2-x}\text{La}_x\text{IrO}_4$  the IMT is accompanied by a moderate renormalization of the electronic correlation substantiated by a reduction of the effective on-site Coulomb repulsion  $U - J$  from 1.6 eV ( $x = 0$ ) to 1.4 eV (metallic regime of  $x = 12.5\%$ ). The progressive closing of the relativistic Mott gap leads to the emergence of connected elliptical electron pockets at  $(\pi/2, \pi/2)$  and less intense features at  $X$  on the Fermi surface. The average ordered magnetic moment is slightly reduced upon doping, but the canted antiferromagnetic state is perturbed on the Ir-O planes located near the La atoms. The substitution of Ir with the nominally isovalent Rh is accompanied by a substantial hole transfer from the Rh site to the nearest-neighbor Ir sites. This shifts down the chemical potential, creates almost circular disconnected hole pockets in the FS, and establishes the emergence of a two-dimensional metallic state formed by conducting Rh planes intercalated by insulating Ir planes. Finally, our data indicate that hole doping causes a flipping of the in-plane net ferromagnetic moment on the Rh plane and induces a magnetic transition from the antiferromagnetic (AF)-I to the AF-II ordering.

DOI: [10.1103/PhysRevB.94.195145](https://doi.org/10.1103/PhysRevB.94.195145)

## I. INTRODUCTION

The recently reported spin-orbital  $J_{\text{eff}} = 1/2$  Mott insulating state in  $\text{Sr}_2\text{IrO}_4$  [1,2] has stimulated a lot of fundamental research aiming to clarify the underlying mechanism responsible for this novel state of matter which arises from the cooperative interplay of the crystal field, spin-orbit coupling (SOC), electron-electron interaction ( $U$ ), and different types of simultaneously active spin-exchange interactions [3–7]. An important aspect of  $\text{Sr}_2\text{IrO}_4$  that also has attracted considerable attention is its similarity with high- $T_c$  cuprate superconductors, such as  $\text{La}_2\text{CuO}_4$ : These two compounds share the same quasi-two-dimensional layered perovskite structure, Ir and Cu have nominal  $d^5$  and  $d^9$  configurations with one effective hole per site, and both compounds are described by a  $S(J_{\text{eff}}) = 1/2$  antiferromagnetic (AF) Heisenberg model [8–11]. Theoretical studies reporting the possible onset of superconductivity in electron-doped  $\text{Sr}_2\text{IrO}_4$  [10,11] have spurred immediate experimental research that has reported the existence of unusual (pseudogap) metallic states in  $\text{Sr}_{2-x}\text{La}_x\text{IrO}_4$ , somehow similar to high- $T_c$  cuprates, but no sign of superconductivity has been found down to very low temperatures for supposedly optimal doping [12–15]. On whether the Fermi surface (FS)

is formed by disconnected Fermi arcs or Fermi lenses is still experimentally uncertain. More generally, electron and hole doping in (relativistic) Mott insulators are one of the most studied and controversial issues in solid-state theory due to the complex impact that excess carriers can have on the competing spin/charge/orbital interactions [16]. In  $\text{Sr}_2\text{IrO}_4$  the study of doping effects can provide important insight on the robustness and tunability of the spin-orbital Mott state and of the canted in-plane antiferromagnetic ordering. This is associated with a controlled doping-induced modulation of the dominant interactions, in particular, SOC and  $U$  as well as with possible changes in the atomic positions (structural distortions) that can have strong repercussions on the electronic and magnetic properties.

Among the different forms of electron and hole doping tested in this system, the most studied ones are the substitution of  $\text{Sr}^{2+}$  with  $\text{La}^{3+}$  (electron doping) and the homovalent heterosubstitution of  $5d^5 \text{Ir}^{4+}$  with  $4d^5 \text{Rh}^{4+}$  (effective hole doping) [15,17–26]. In one of the first studies, Lee and co-workers conducted a systematic investigation of La, Rh, and Ru doping in  $\text{Sr}_2\text{IrO}_4$  by means of optical spectroscopy and found that the  $J_{\text{eff}} = 1/2$  state remains spectroscopically robust upon doping and that in all cases doping induces an insulator-to-metal transition (IMT) for moderately low dopant concentrations ( $\approx 5\%$ ) [19]. They have also suggested that the IMT is associated with subtle alterations of the strength of  $U$

\*Corresponding author: [cesare.franchini@univie.ac.at](mailto:cesare.franchini@univie.ac.at)

and SOC [19]. This hypothesis has been studied more recently in a combined angle-resolved photoelectron spectroscopy (ARPES) and tight-binding study of La-doped  $\text{Sr}_2\text{IrO}_4$  where the authors have concluded that an optimal agreement between experiment and calculation can be achieved assuming a fast quenching of  $U$  from 2 to 0 eV across the transition [15]. On the other hand, the idea that a reduction of the SOC should be responsible for the closing of the Mott gap in the Rh-doped sample has been revised by Cao and co-workers: They have shown that Rh doping effectively corresponds to hole doping and therefore in this case the IMT can be explained by a band-filling mechanism [21]. In our paper we reconcile these two apparently conflicting interpretations and will show that the effective hole-doping mechanism is assisted by the different SOC strengths in Rh and Ir.

Substitutional doping also has a significant influence on the magnetic order. Upon La doping, a complex phase diagram was proposed showing the weakening of the long-range AF order and the appearance of a spin-glass-like phase beyond a critical La concentration [24]. Rh doping was found to induce a magnetic transition from the AF-I to the AF-II state involving the in-plane flipping of the net ferromagnetic (FM) moment [22,23] as shown in Fig. 1(b). Despite the relatively large amount of experimental studies on doped  $\text{Sr}_2\text{IrO}_4$  first-principles calculations were not reported to date. In this paper, we study the evolution of the spin-canted Mott state in  $\text{Sr}_2\text{IrO}_4$  as a function of La and Rh dopings using relativistic density functional theory (DFT) with the inclusion of an on-site Hubbard  $U$ , the same scheme that we have used

for the description of the ground-state electronic and magnetic interactions in the undoped compound [6]. Doped Mott insulators generally are studied using model Hamiltonian schemes as these methods are designed to describe the role of strong correlation across the IMT in particular band renormalization and the transfer of spectral weight, which are not accessible by single-particle approaches. However, the combined ARPES and tight-binding study of de la Torre *et al.* [15] indicates that the band structure of doped  $\text{Sr}_2\text{IrO}_4$  is sufficiently well described using single-particle-like dispersions suggesting that a single-particle band theory, such as DFT +  $U$  might be a suitable approximation in this case. We will carefully address this point in this paper.

From an *ab initio* perspective the *realistic* treatment of doping requires the employment of large supercells (SCs), and for a one-to-one comparison with available ARPES electronic structure it is necessary to map the band structure calculated in the supercell into an effective band structure (EBS) projected in the Brillouin zone of the primitive cell. To this aim we used the band-structure unfolding method introduced a few years ago by Popescu and Zunger [27,28] and recently incorporated in the Vienna *ab initio* simulation package (VASP) [29,30]. With this approach we have computed the EBS and FS of La- and Rh-doped  $\text{Sr}_2\text{IrO}_4$  at different concentrations across the IMT, and the obtained results are in reasonable agreement with the available ARPES spectra. Our data suggest that La doping leads to a moderate reduction of the effective Coulomb interaction  $U_{\text{eff}} = U - J$  from 1.6 eV, the optimum value in the undoped system, to 1.4 eV at the electron-doping concentration of  $x = 12.5\%$ . The upshift of the chemical potential upon electron doping and the renormalization of the electronic correlation result in a metallic state, however, we fail to predict the merging of the lower and upper Hubbard bands at low electron-doping concentrations at the optimum  $U_{\text{eff}}$  values. The complete closing of the gap is achieved for smaller values of  $U_{\text{eff}}$  ( $\approx 0.8$  eV). As already mentioned, although Rh in  $\text{Sr}_2\text{RhO}_4$  is isoelectronic with Ir in  $\text{Sr}_2\text{IrO}_4$ , our DFT results confirm the experimental conclusions that Rh substitution in  $\text{Sr}_2\text{IrO}_4$  acts as a hole donor shifting up the valence bands and creating a hole pocket around the X point.

In the next section we will provide the technical details on the computational methods and setup. The results will be presented and discussed in Sec. III and summarized in Sec. IV.

## II. COMPUTATIONAL DETAILS

Our first-principles calculations including  $U$  and SOC were performed using the projector augmented-wave method [31] as implemented in VASP [32,33]. The Perdew-Burke-Ernzerhof [34] approximation was employed for the exchange-correlation functional. Plane waves have been included up to an energy cutoff of 400 eV. A  $4 \times 4 \times 2$   $k$ -point grid was used to sample the Brillouin zone for the supercell calculations, which has been increased to  $6 \times 6 \times 2$   $k$  point in the conventional cell. For the undoped case, we used an effective  $U_{\text{eff}} = U - J = 1.6$  eV on the Ir site, computed using the constrained random-phase approximation (cRPA), which yields a very good account of the ground-state electronic and magnetic properties [6]. The cRPA has also been employed

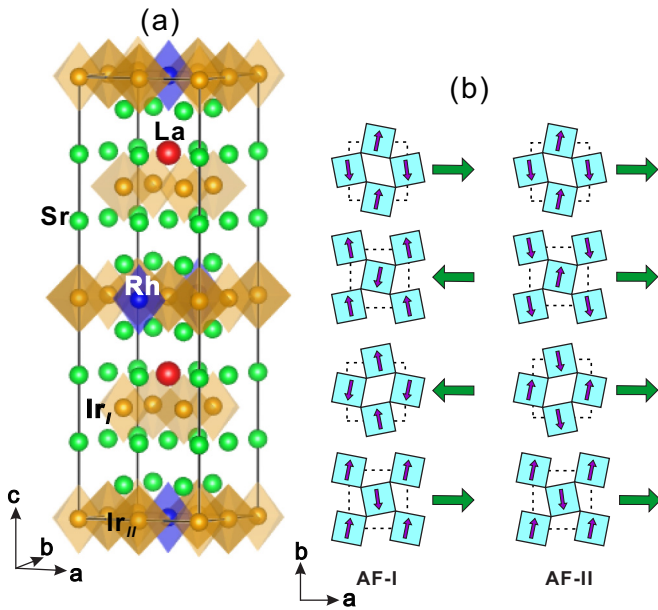


FIG. 1. (a) Ball and stick model of a supercell adopted in the present paper to model  $\text{Sr}_{2-x}\text{La}_x\text{Ir}_{1-y}\text{Rh}_y\text{O}_4$ , showing the substitutional  $\text{Sr} \rightarrow \text{La}$  (dark spheres) and  $\text{Ir} \rightarrow \text{Rh}$  (dark octahedra) sites. Two different kinds of Ir atoms can be identified:  $\text{Ir}_{II}$ , nearest neighbor to Rh, and  $\text{Ir}_I$ . Oxygen atoms are not displayed. (b) Schematic plot of the canted AF-I and AF-II orderings, showing both the ordered AF moments (thin blue arrows) and the flipping of the net in-plane ferromagnetic moment (thick green arrows).

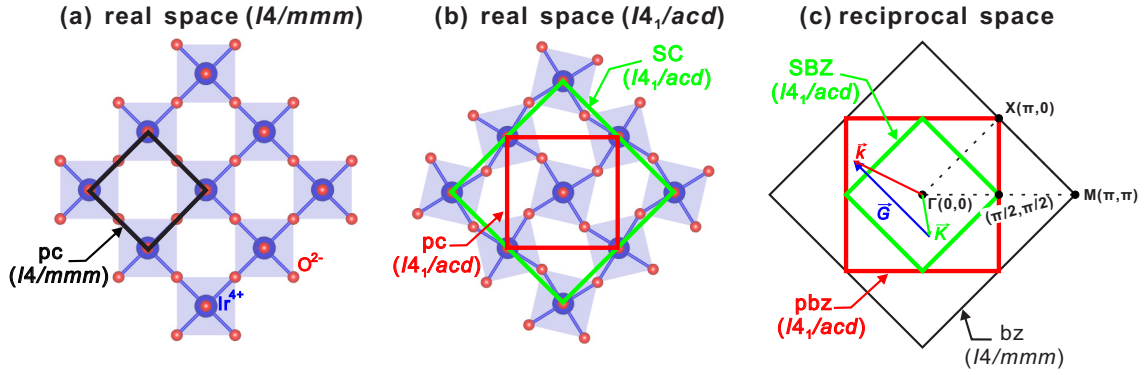


FIG. 2. The relation between primitive cell (pc) and SC in real space for (a) the undistorted ( $I4/mmm$ ) and (b) the distorted ( $I4_1/acd$ ) structures. (c) The corresponding primitive (pbz) and supercell Brillouin zones (SBZs) and their associated wave-vectors  $\vec{k}$  and  $\vec{K}$  connected by the reciprocal lattice vector  $\vec{G}$  of the supercell are illustrated. Note that in (c) the fractional coordinates of high-symmetry points are displayed using  $I4/mmm$  notation in units of  $1/a_0$  with  $a_0$  being the  $ab$ -plane lattice constant of the undistorted structure.

to compute the  $U_{\text{eff}}$  in the high-doping regime ( $x = 12.5\%$ ). For the Rh-doping case, we have included an on-site  $U_{\text{eff}} = 1.2$  eV on the Rh sites, estimated by cRPA [35]. For the cRPA calculations we have employed the same setup as in our previous study on bulk  $\text{Sr}_2\text{IrO}_4$  [6], following the Kubo formalism derived by Kaltak [36]. The Kohn-Sham orbitals are projected onto maximally localized Ir  $t_{2g}$  Wannier functions using the WANNIER90 code [37] and the VASP2WANNIER90 interface [38]. The screening channels within the  $t_{2g}$  target states are removed in calculating the independent polarizability. For both phases, undoped and high-doping regimes, the cRPA  $U_{\text{eff}}$  was calculated using the same conventional cell containing 56 atoms (8 Ir atoms); in the doped case we have substituted one Sr atom with one La atom. Overall we have constructed 24 Wannier functions from the  $t_{2g}$ -like Bloch states.

In order to fully account for the doping effects on the electronic structure of doped  $\text{Sr}_2\text{IrO}_4$ , we employed the supercell approach. The supercell ( $\sqrt{2} \times \sqrt{2} \times 1$ ) with 112 ions, depicted in Fig. 1(a), was constructed based on the experimental unit cell with  $I4_1/acd$  symmetry [39] as shown in Fig. 2(b). For the La doping ( $\text{La}^{3+}$  for  $\text{Sr}^{2+}$ ) [18] the chemical formula becomes  $\text{Sr}_{32-y}\text{La}_y\text{Ir}_{16}\text{O}_{64}$  with  $y$  being the number of  $\text{La}^{3+}$  ions in the supercell. Thus, substitution of one (two)  $\text{Sr}^{2+}$  by  $\text{La}^{3+}$  corresponds to a La-doping concentration  $y$  of 3.125% (6.25%). It should be noted that the nominal electron doping counted per Ir site is doubled due to the stoichiometry of  $\text{Sr}_2\text{IrO}_4$  [15], yielding electron-doping concentrations of  $x = 2y = 6.25\%$  and  $12.5\%$ , respectively. With respect to the concentration  $x$ , the general chemical formula for La doping reads  $\text{Sr}_{2-x}\text{La}_x\text{IrO}_4$ . For the Rh doping ( $\text{Rh}^{3+}$  for  $\text{Ir}^{4+}$  in the supercell  $\text{Sr}_{32}\text{Ir}_{16-x}\text{Rh}_x\text{O}_{64}$ ) [21], substitution of one (two)  $\text{Ir}^{4+}$  by  $\text{Rh}^{3+}$  results in nominal hole doping on the Ir site of  $x = 6.25\%$  (12.5%). To avoid confusion, we use  $x$  to label the electron- (hole-) doping concentrations throughout the paper. Unless explicitly stated, all supercell calculations were performed by fully relaxing the atomic positions at a fixed volume, corresponding to the experimental volume of the undoped compound, in order to preserve local structural effects of the dopant atoms.

To analyze the effects of doping on the band structure of the employed supercells, we have adopted the unfolding technique recently implemented in VASP [29,30]. In fact, calculations based on the supercell approach with a unit cell  $N$  times larger than the primitive cell, lead to a down-folded Brillouin zone that, in most cases, makes it difficult to interpret directly the resulting band structures. An unfolding technique is required in order to obtain a clearer description of the band structure. The relation,

$$\vec{k} + \vec{g} = \vec{K} + \vec{G} \quad (1)$$

describes the folding of the reciprocal space, mapping a wave-vector  $\vec{K}$  of the supercell into  $N$  wave-vectors  $\vec{k}$  in the pbz by means of the reciprocal lattice vectors  $\vec{g}$  and  $\vec{G}$  of the primitive and supercells, respectively [see Fig. 2(c)]. The projection  $P_{\vec{K}m}(\vec{k})$  of the eigenstates  $|\Psi_{\vec{K}m}\rangle$  of the supercell into eigenstates  $|\psi_{\vec{k}n}\rangle$  of the primitive cell, where  $m$  and  $n$  are energy-band indices, provides an EBS in the pbz starting from eigenvalues calculated in the SBZ. As proved by Popescu and Zunger [27,28], the projection  $P_{\vec{K}m}(\vec{k})$ , called the Bloch character, can be written in terms of the plane-wave coefficients of the supercell eigenstates only. In fact, given Eq. (1), the eigenstates of the supercell can be written as

$$\begin{aligned} \Psi_{\vec{K}m}(\vec{r}) &= \sum_{\vec{G}} C_{\vec{K}+\vec{G},m} e^{i(\vec{K}+\vec{G})\cdot\vec{r}} \\ &= \sum_{\vec{k}} \sum_{\vec{g}} C_{\vec{k}+\vec{g},m} e^{i(\vec{k}+\vec{g})\cdot\vec{r}}. \end{aligned} \quad (2)$$

Therefore, the Bloch character can be obtained from the supercell calculation alone, and no primitive cell calculations are required because of the relation,

$$P_{\vec{K}m}(\vec{k}) = \sum_n |\langle \Psi_{\vec{K}m} | \psi_{\vec{k}n} \rangle|^2 = \sum_{\vec{g}} |C_{\vec{k}+\vec{g},m}|^2. \quad (3)$$

The spectral function  $A(\vec{k}, E)$  can hence be calculated as

$$A(\vec{k}, E) = \sum_m P_{\vec{K}m}(\vec{k}) \delta(E_m - E), \quad (4)$$

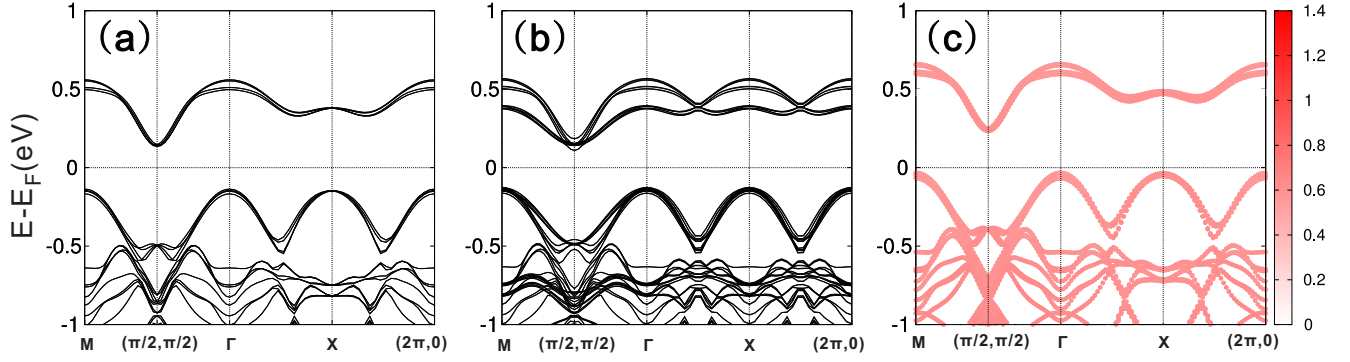


FIG. 3. Band structure of (a) a primitive cell and (b) a supercell. (c) The EBS calculated from the unfolding method. Note that the color bar in (c) represents the Bloch character given by Eq. (3). The high-symmetry points here are consistent with the primitive  $I4_1/mmm$  notation displayed in Fig. 2(c).

providing a directly comparison of the calculated EBS with ARPES experiments in the reciprocal space of the primitive cell.

To validate and demonstrate the applicability of the unfolding scheme, we show in Fig. 3 a comparison between the ground-state band structure of undoped  $\text{Sr}_2\text{IrO}_4$  in the primitive  $I4_1/acd$  cell [Fig. 3(a)] and in the  $I4_1/acd$  supercell [Fig. 3(b)] together with the EBS of the supercell unfolded into the primitive cell [Fig. 3(c)]. The primitive cell band structure exhibits the well-known relativistic Mott  $J_{\text{eff}} = 1/2$  state formed by one filled and one empty band, usually referred to as the lower and upper relativistic Mott-Hubbard bands [(LHB) and (UHB), respectively], which are separated by a small band gap of about 0.3 eV [1]. The EBS of the undoped supercell shown in Fig. 3(c) reproduces well this behavior: The EBSs are formed by sharp bands reflecting the fact that the eigenstates of the primitive cell can contribute either fully or not at all to a given supercell eigenstate. Dopant atoms clearly will disrupt this one-to-one correspondence between supercell and primitive cell eigenstates introducing mixed contributions represented by intermediate values for the Bloch characters and, hence, broadened bands.

### III. RESULTS AND DISCUSSION

#### A. La doping

We start this section by discussing the relation between doping and electron-electron correlation. The ARPES spectra clearly indicate a fast collapse of the relativistic Mott gap and the appearance of a large Fermi surface at relatively low-doping levels [15]. As La doping effectively induces excess electrons in the system, one would expect that the strength of the electron-electron correlation measured in terms of  $U_{\text{eff}}$  should decrease with increasing doping concentration as a consequence of the increased screening from the metallic states. Considering that the IMT occurs at rather low doping (few percent) one would expect that the  $U_{\text{eff}}$  would not change much across the transition. In contrast to this expectation, however, previous tight-binding calculations suggested that only a complete quenching of the Coulomb repulsion  $U$  from an ideal value of 2.0 eV, assumed for the undoped case, to 0 eV at  $x = 0.1$  reproduced the experimental ARPES data. To verify the reliability of this conjecture we have computed  $U_{\text{eff}}$

fully *ab initio* using cRPA for the largest doping concentration considered in our paper  $x = 12.5\%$  using the conventional cell containing 56 atoms. We found  $U_{\text{eff}} = 1.4$  eV, implying that  $U_{\text{eff}}$  is only moderately affected by doping at these low concentrations (see Fig. 4). Assuming a linear decrease in  $U_{\text{eff}}$  upon doping a full suppression of  $U_{\text{eff}}$  would occur at very large doping of  $x \approx 80\%$ . A conceptually similar reduction of electronic correlation effects due to electron doping, analyzed in terms of the changes in the mass enhancement factor, was recently reported for La-doped  $\text{Sr}_2\text{RhO}_4$  [40].

With this set of *optimum* values of  $U_{\text{eff}}$  at hand, we have computed the EBS, FS, and density of states (DOS) for increasing doping concentrations:  $x = 0, 6.25\%$ , and  $12.5\%$ . The results, shown in Fig. 5, clearly show that, upon La doping,  $\text{Sr}_2\text{IrO}_4$  undergoes an IMT associated with a progressive reduction of the separation between the LHB and the UHB and the emergence of a structured FS. Already at the lowest-doping concentration  $x = 6.25\%$ , the bottom of the UHB crosses the Fermi energy at  $(\pi/2, \pi/2)$  forming elliptical spots in the FS. By increasing doping the elliptical electron pockets become sharper, and additional features appear in the FS around the X point arising from the doping-induced spectral weight broadening at the top/bottom of the lower/upper Hubbard bands. This is in modest agreement with the available ARPES experiments [12–15], specifically some differences are noticeable at the X point and at  $(\pi/2, \pi/2)$ . In the experiments, the distance between the upper and the lower

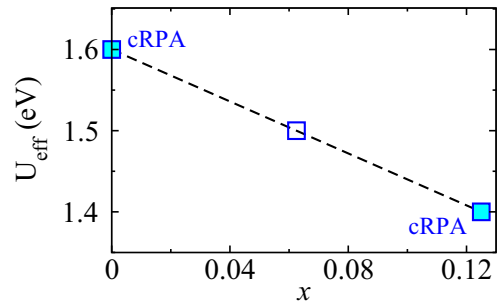


FIG. 4. Effective electron-electron interaction  $U_{\text{eff}}$  as a function of electron-doping concentrations  $x$ . The filled symbols correspond to the actual values computed by cRPA, whereas the open symbol is the interpolated value of  $U_{\text{eff}}$  for the lowest-doping level  $x = 6.25\%$ .



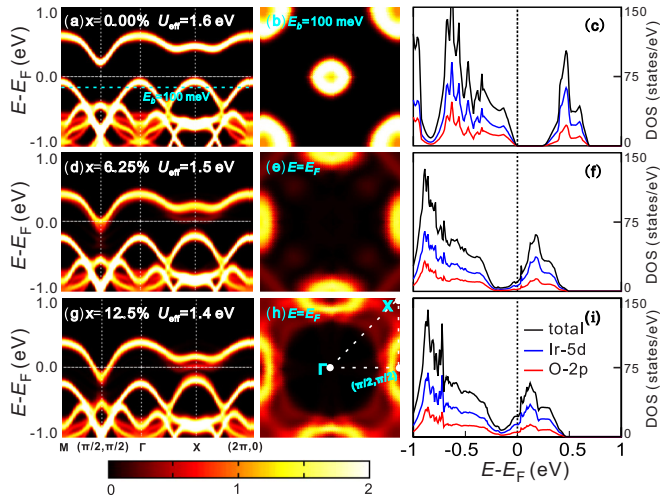


FIG. 5. Doping-induced IMT in  $\text{Sr}_2\text{IrO}_4$  in terms of EBS, FS, and total and Ir-5d- and O-2p-projected DOS at different electron-doping concentrations  $x$ : (a)–(c)  $x = 0$ ; (d)–(f)  $x = 6.25\%$ ; (g)–(i)  $x = 12.5\%$ . The Fermi level is set at zero. For the insulating  $x = 0$  case the FS is replaced by an isoenergy ( $E_b = 100$  meV) contour plot.

Hubbard bands closes upon doping, and as the lower and upper Hubbard bands merge, a Dirac cone develops at the  $(\pi/2, \pi/2)$  point. In our simulations this only starts to happen at much larger concentrations beyond  $x = 12.5\%$  or for smaller values of  $U_{\text{eff}}$  (see Fig. 6). Furthermore in the experiments the valence-band edge at the X point moves above the Fermi level. If we keep the  $U_{\text{eff}}$  largely fixed, this feature is not observed in our theoretical calculations, although a doping-induced broadening of the lower/upper Hubbard bands is visible. We believe that the main reason for this erroneous result is the inadequacy of the DFT +  $U$  method. In the present case, the conduction band at the X point is nonlocalized, similar to conventional semiconductors. Likewise the top most valence-band state at the X point is itinerant. Using a simple local correction  $U$  can open the band gap between the lower and the upper Hubbard bands, but it is not able to deal properly

with the intricate details of nonlocalized itinerant states. The minimum complexity required to describe band-gap narrowing upon doping is  $GW$ , but  $GW$  for the system sizes considered here is yet very difficult, and we relegated this to future work.

To clarify how  $U_{\text{eff}}$  changes the band structure, we report in Fig. 6 the EBSs with projected spectral weight computed for different values of  $U_{\text{eff}}$  at  $x = 6.25\%$  and  $x = 12.5\%$ . Specifically, we have considered  $U_{\text{eff}} = 1.5, 1.0, 0.75$ , and  $0.5$  eV for  $x = 6.25\%$  and  $U_{\text{eff}} = 1.4, 0.8, 0.5$ , and  $0.0$  eV for the largest concentration  $x = 12.5\%$ . Clearly, the value of  $U_{\text{eff}}$  affects the robustness of the  $J_{\text{eff}} = 1/2$  state. Upon decreasing  $U_{\text{eff}}$  (from left to right in Fig. 6) the separation between the LHB and the UHB is progressively reduced as a result of the downward shift of the UHB, especially near the  $(\pi/2, \pi/2)$  point and an upward shift of the LHB around the X point. Moreover, the reduction of  $U_{\text{eff}}$  strengthens the intensity of the Dirac cone at  $(\pi/2, \pi/2)$  around  $-0.2$  eV and influences the intensity of the spectral weight at the X and  $(\pi/2, \pi/2)$  points. Obviously reducing  $U$  would indeed reproduce the experimental results, for instance, the emergence of the Dirac cone at  $(\pi/2, \pi/2)$  and a shift of the valence-band edge at X above the Fermi level. However, from a first-principles perspective this is certainly unsatisfactory since we cannot justify the rapid reduction of  $U$  with doping.

After discussing the origin of the doping-induced IMT we conclude this section by discussing the effect of La doping on the structure and on the magnetic ordering. Due to the smaller ionic radius of  $\text{La}^{3+}$  compared with  $\text{Sr}^{2+}$ , the inclusion of  $\text{La}^{3+}$  induces small local distortions ( $\approx 2\%$ ) near the La site due to the stronger electrostatic  $\text{La}^{3+}$ -O attraction as compared to  $\text{Sr}^{2+}$ -O leading to a smaller La-O distance as compared to Sr-O in the undoped sample and to a small expansion of the Ir-O apical bond length within the  $\text{IrO}_6$  octahedron as schematically shown in Fig. 7. The structural modifications of one to two unit cells away from the La sites are found to be almost negligible ( $< 1\%$ ). We found that the effects of these structural rearrangements on the electronic structure (not shown) are minimal. Conversely doping and structural relaxation perturbed the ordered canted state characteristic of the undoped phase. Our data indicate that, apart from

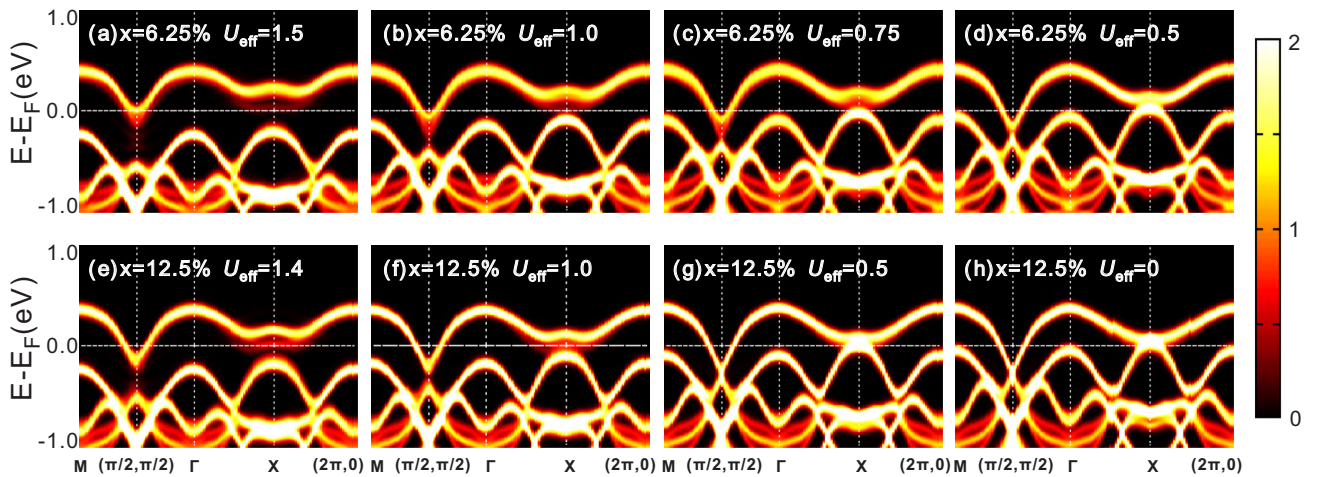


FIG. 6. The EBS of La-doped  $\text{Sr}_2\text{IrO}_4$  as a function of the effective Hubbard interactions  $U_{\text{eff}}$  (eV) for the electron-doping concentrations  $x = 6.25\%$  and  $12.5\%$ . The color coding indicates the spectral function calculated by Eq. (4).

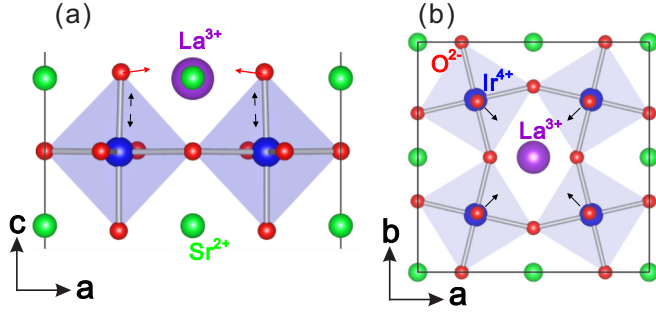


FIG. 7. (a) Side and (b) top views of the structural relaxations around the  $\text{La}^{3+}$  ion manifested by tilting and stretching of the  $\text{IrO}_6$  octahedra (highlighted schematically by the arrows).

a relatively small decrease in the average ordered moment, La doping leads to a local disruption of the canted ordering on the Ir planes closer to the La impurity. This is in line with the experimental observation of a weakening of the long-range-canted AF order [24] upon La doping.

### B. Rh doping

Following the same procedure adopted for the electron-doping case we have studied the evolution of the electronic and magnetic states of  $\text{Sr}_2\text{IrO}_4$  upon hole doping. As mentioned in the Introduction effective hole doping can be achieved by replacing  $5d$   $\text{Ir}^{4+}$  with the corresponding nominally isovalent  $4d$  element  $\text{Rh}^{4+}$ , situated directly above Ir in the periodic table. The parent Rh compound  $\text{Sr}_2\text{RhO}_4$  is isostructural to  $\text{Sr}_2\text{IrO}_4$  but exhibits a smaller in-plane octahedral rotation angle of  $\approx 9.7^\circ$  [41]. However,  $\text{Sr}_2\text{RhO}_4$  is a paramagnetic correlated metal [41–43], characterized by a weaker SOC strength combined with a more effectively screened Coulomb interaction between  $\text{O}-2p$  and  $\text{Rh}-4d$  electrons as compared to  $\text{Sr}_2\text{IrO}_4$  [35]. This is substantiated by a smaller  $U_{\text{eff}}$  for the Rh  $4d$  states 1.2 eV [35] as compared to  $5d$  Ir 1.6 eV [6]; we have used this value for our DFT +  $U$  analysis. The calculations for  $\text{Sr}_2\text{Ir}_{1-x}\text{Rh}_x\text{O}_4$  were performed in large supercells of the same size as those used for the electron-doping case, suitable to model the low-doping regimes of  $x = 6.25\%$  and  $12.5\%$ . The doping-induced structural changes are generally small: We found a slight increase in the tetragonal distortion  $c/a$  within the  $\text{RhO}_6$  octahedron ( $c$  and  $a$  here refer to the apical and in-plane Rh-O bond lengths in the  $\text{RhO}_6$  sublattice) and a decrease in octahedral rotation angle  $\alpha$  compared to  $\text{Sr}_2\text{RhO}_4$  (the structural data are listed in Table I).

It was proposed that  $\text{Ir} \rightarrow \text{Rh}$  chemical substitution leads to hole transfer from Rh to Ir ideally leading to the formation of  $\text{Ir}^{5+}$  and  $\text{Rh}^{3+}$  ions [17,21,22]. Although formally correct, this picture is rather simplified as it does not consider possible changes in the  $\text{Ir}-d/\text{O}-p$  hybridization and does not account for the presence of the two inequivalent  $\text{Ir}_I$  and  $\text{Ir}_{II}$  sites in the compound (see Fig. 1). To clarify this issue, in Fig. 8 we show our calculated charge-density difference between the doped and the undoped samples within the plane containing the substitutional Rh ion. Here the intensity map offers a simple way to visualize the doping-induced changes in the charge-density distribution in terms of charge transfer from the dark to the

TABLE I. The Rh-doping ( $x = 6.25\%$ ) effect on the structural distortions of the  $\text{RhO}_6$  octahedra and their first nearest-neighbor ( $1nn$ )  $\text{Ir}_{II}\text{O}_6$  octahedra.  $c$  (a) (in Å) represents the apical (in-plane)  $M-\text{O}$  ( $M = \text{Ir}$  or  $\text{Rh}$ ) bond length.  $\alpha$  indicates the in-plane octahedral rotation angle (degree). For comparison, the calculated values for the bulk  $\text{Sr}_2\text{IrO}_4$  and  $\text{Sr}_2\text{RhO}_4$  also are given. The  $\text{Ir}_I\text{O}_6$  octahedra remain almost unchanged (not listed). All data were obtained by DFT +  $U$  + SOC calculations. For  $\text{Sr}_2\text{RhO}_4$  we used the experimental lattice parameters reported in Ref. [44].

	$\text{Sr}_2\text{IrO}_4$	$\text{Sr}_2\text{RhO}_4$	$\text{Sr}_2\text{Ir}_{1-x}\text{Rh}_x\text{O}_4$	
	$\text{IrO}_6$	$\text{RhO}_6$	$\text{Ir}_{II}\text{O}_6$	$\text{RhO}_6$
$c$	2.071	2.067	2.062	2.104
$a$	1.992	1.969	1.977	2.007
$c/a$	1.040	1.050	1.043	1.048
$\alpha$	$13.22^\circ$	$11.82^\circ$	$12.99^\circ$	$12.75^\circ$

white regions: The electron transfer involves an accumulation of electronic charge around Rh and (to a lesser extent) O sites and a substantial modification of the  $\text{Ir}-d/\text{O}-p$  hybridization, in particular, along the  $\text{Rh}-\text{O}-\text{Ir}-\text{O}-\text{Rh}$  directions. One can clearly identify the difference between the two kinds of iridium atoms:  $\text{Ir}_{II}$  ions, nearest neighbors to Rh, are surrounded by a dark cloud indicating that these atoms donate electron charges to Rh and O, whereas the charge density around the  $\text{Ir}_I$  ions (all other Ir sites in the supercell) remain essentially unaffected. This disproportionation between inequivalent Ir sites also is well

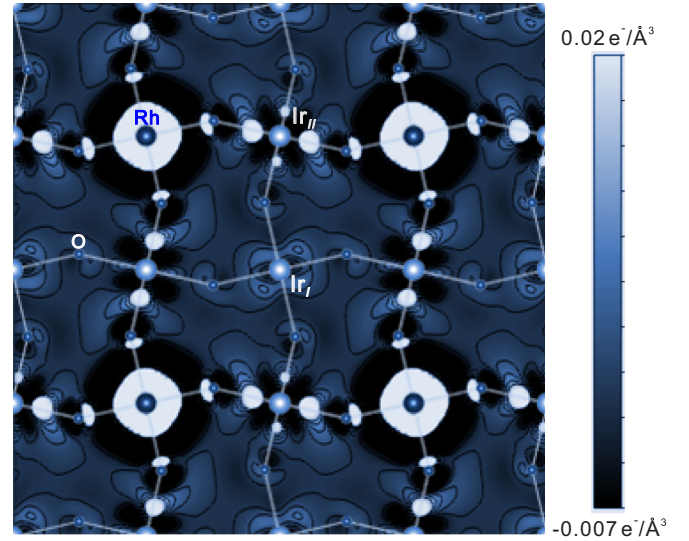


FIG. 8. Charge density difference between the doped  $x = 6.25\%$  and the undoped  $x = 0$  cases within the plane containing the Rh-dopant ion. The gray (blue) intensity scale delineates the charge-transfer process driven by doping which is associated with an electron transfer from the dark to the white areas. Upon Rh doping, type-II iridium ions give away a fraction of their  $t_{2g}$  electrons, which are mostly accumulated at the Rh sites, resulting in an effective hole doping. The  $\text{Ir}-d/\text{O}-p$  hybridization along the  $\text{Rh}-\text{O}-\text{Ir}-\text{O}-\text{Rh}$  bond directions is also strongly influenced by doping, whereas the charge distribution around the  $\text{Ir}_I$  atoms and around the non-nearest-neighbor O atoms remain almost unchanged.

captured by the DOS shown in Fig. 9 (middle panels):  $\text{Ir}_I$ -type atoms preserve a  $t_{2g}$ -projected DOS (shadow areas) almost identical to the Ir atoms in the undoped sample [Fig. 9(c)] with an essentially insulating character. In contrast,  $\text{Ir}_{II}$ - $t_{2g}$  states are pushed above the Fermi energy, and the peak above the Fermi energy is progressively depleted by increasing doping concentration.

We will now discuss the changes in the density of states in detail showing that the transition to the metallic state is caused by the reduced SOC at the Rh site as well as a downshift of Rh  $4d$  states compared to the Ir  $5d$  states. Figure 9(f) clearly shows that the shape of the DOS at the Rh atoms closely resembles that at the Ir atoms, however, the Rh  $t_{2g}$  states are located at more negative binding energies than the Ir  $t_{2g}$  states. This is well understood: As a result of relativistic effects, the Ir  $6s$  states are closer to the nucleus, screening it and pushing the Ir  $5d$  states upward compared to the Rh  $4d$  states; for isolated atoms the effect is typically 0.5 eV, here, the Rh  $4d$  states are shifted downward by about 0.2 eV compared to the Ir  $5d$  states. The second important point is that spin-orbit coupling is much reduced in Rh compared to Ir. Thus the gap between the lower and the upper Hubbard  $t_{2g}$  bands closes: Clearly the  $t_{2g}$  states that are located above the Fermi level for Ir (peak around 0.5 eV) shift into the gap shown by the prominent midgap Rh  $t_{2g}$  peak at 0.1 eV. Since Rh has a very small spin-orbit coupling these states even overlap with the lower Hubbard band and become partially occupied. Hence the oxidation of

Rh is  $\text{Rh}^{4-\delta}$  with  $\delta$  being the number of electrons per site transferred to Rh from the neighboring Ir ions. An oxidation state of  $\text{Rh}^{3+}$  is not quite reached in our calculations as this would imply a larger occupation of the Rh upper Hubbard band. However, our DOS data and Bader charge analysis indicate that  $\delta$  is  $\approx 0.7e^-$ . An additional important point is that the neighboring in-plane  $\text{Ir}_{II}$  atoms strongly hybridize with the Rh atom [see Figs. 9(f) and 9(i)]. As already shown in Fig. 8, each  $\text{Ir}_{II}$  atom donates the charge  $\delta/2$  to the Rh upper Hubbard band. Hence, Rh creates a fractional hole in the Ir lower Hubbard band, and the Fermi level is shifted into the lower Hubbard Ir band. This is in agreement with a recent DFT +  $U$  study reporting that  $\text{Ir} \rightarrow \text{Rh}$  substitution is almost isoelectronic and introduces impurity states of predominantly Rh character in the gap region [45]. Finally, it is important to note that since Rh substitution only affects the in-plane Ir atom, doping results in an essentially two-dimensional metallicity; the planes containing only  $\text{Ir}_I$  atoms retain a predominantly insulating character, very similar to the undoped situation. It should be noted, however, that the specific type of metallic state induced by Rh doping will depend on the way doping is introduced into the systems and, from a computational point of view, on the choice of the supercell adopted in the simulation.

The hole-doping-induced IMT is described in Fig. 9 in terms of the EBS, FS, DOS, and magnetic ordering. It can be seen that the insulating state already is perturbed at the lowest-doping concentration due to an upward shift of the LHB driven

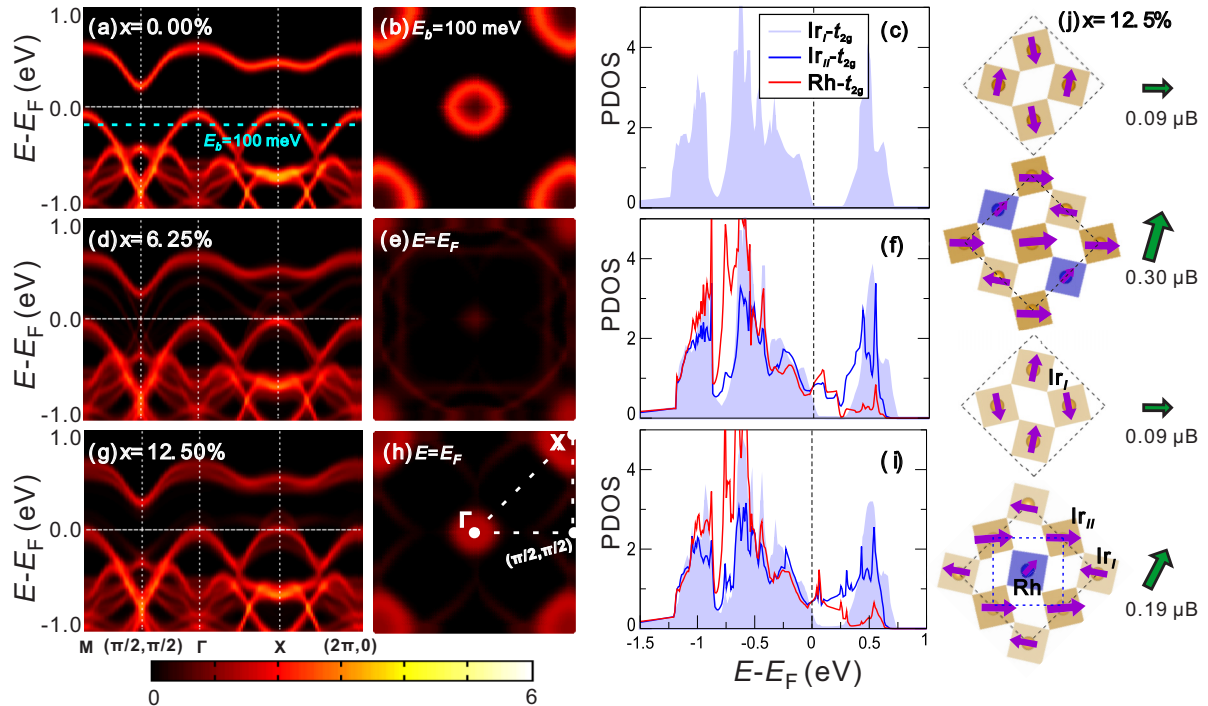


FIG. 9. Electronic and magnetic properties of Rh-doped  $\text{Sr}_2\text{IrO}_4$ . First column: EBS of (a) undoped and Rh-doped  $\text{Sr}_2\text{IrO}_4$  with the nominal hole concentration (d)  $x = 6.25\%$  and (g)  $x = 12.5\%$ . The color code represents the intensity of the spectral function. Second column: (b) constant energy contour of undoped  $\text{Sr}_2\text{IrO}_4$  at the binding energy  $E_b = 100$  meV and Fermi surfaces for (e)  $x = 6.25\%$  and (h)  $x = 12.5\%$ . Third column:  $t_{2g}$  DOS (states  $\text{eV}^{-1} \text{atom}^{-1}$ ) projected on the Rh,  $\text{Ir}_I$ , and  $\text{Ir}_{II}$  sites for (c)  $x = 0$ , (f)  $6.25\%$ , and (i)  $12.5\%$ . Fourth column: schematic plot of the AF-II-like magnetic ordering emerging upon doping similar to the ideal AF-II ordering shown in Fig. 1 (given for  $x = 12.5\%$ , a similar ordering is obtained at the lower-doping concentration). The magnitude and direction of the resulting planar magnetic moment obtained by DFT +  $U$  + SOC also are given.



by the charge transfer process described above, involving electron transfer from the  $\text{Ir}_{II}$  sites to the Rh ions. The LHB crossing at the Fermi energy yields the emergence of hole pockets at  $X$  and  $\Gamma$  and the formation of a FS. These results, obtained for fixed (i.e., not doping concentration-dependent) values of  $U_{\text{eff}}$  for Rh and Ir, are generally in good agreement with available ARPES data [21,25]; the only exception is the position of the valence-band maxima at  $\Gamma$  that is not well described by DFT +  $U$  (and  $GW$  [46]) as already mentioned previously. The UHB preserves its fundamental structure upon doping, but it loses spectral intensity and becomes more disperse, suggestive of spectral weight across the gap [25]. This also is reflected in the weakening of the corresponding DOS with increasing doping [Figs. 9(f) and 9(i)] and compatible with the electron transfer process.

We conclude by reporting the impact of Rh doping on the magnetic ordering. It is well established [2] that the magnetic ground state of undoped bulk  $\text{Sr}_2\text{IrO}_4$  exhibits the AF-I-type ordering shown in Fig. 1(b), characterized by an in-plane *ab*-canted antiferromagnetic arrangement in which the net in-plane FM moments are aligned with a right-left-left-right pattern along  $c$  [see AF-I in Fig. 1(b)]. Upon Rh doping, in the range of  $0.05 < x < 0.15$ , it is experimentally found [22,23] that the interlayer AF-I coupling changes to FM giving rise to the so-called AF-II-type state, also depicted in Fig. 1(b). Our DFT +  $U$  + SOC calculations indicate that doping indeed strongly perturbs the AF-I-type ordering and establishes a new spin pattern similar to the AF-II. As an example, in Fig. 9(j) we show the obtained magnetic ground state for the Rh-doping concentration of  $x = 12.5\%$ : With respect to the parent AF-I state here the net in-plane moments are subjected to a  $100^\circ$  rotation and get closer to an AF-II arrangement. This spin configuration is found to be 4 meV per formula unit more stable than the AF-I one.

#### IV. CONCLUSIONS

We have investigated the effects of dilute La (electron) and Rh (hole) doping on the electronic, structural, and magnetic properties of  $\text{Sr}_2\text{IrO}_4$  by means of magnetically noncollinear (DFT +  $U$  + SOC)-based supercell calculations combined with the unfolding band-structure technique. We show and analyze the effective band structure, Fermi surfaces, density of states, and evolution of the magnetic ordering.

For La doping, our data provide only a partly satisfactory interpretation of the IMT. Electron doping causes an increase in the chemical potential and drives a moderate renormalization

of the electron-electron interaction quantified by a reduction of the on-site Coulomb interaction  $U_{\text{eff}}$  with doping from 1.6 eV at  $x = 0$  to 1.4 eV at  $x = 12.5\%$ . Upon doping, a metallic state emerges in our simulations, however, the vanishing of the gap between the lower and the upper Hubbard bands cannot be reproduced satisfactorily. Therefore, some features are not captured in our simulations, for instance, we fail to observe Dirac-like states at  $(\pi/2, \pi/2)$ . Only if  $U$  is reduced significantly ( $\approx 0.5$  eV), does the Dirac cone emerge as the lower and upper Hubbard bands approach and the gap closes, in accordance with previous model studies performed at  $U = 0$  [15]. From a first-principles perspective this is certainly not satisfactory, implying that the one-electron methods used here are not sufficient to reproduce the experiments satisfactorily. As for the magnetic properties, although the magnitude of the local moment is only marginally affected by doping, the characteristic canted AF-I state is locally perturbed in the vicinity of the La site, and for doping concentrations of  $x > 12.5\%$  a regular long-range-canted AF-I pattern is lost.

For the Rh-doping case our data demonstrate that Rh doping is responsible for a charge redistribution involving predominantly a fractional electron transfer to the Rh sites from the nearest-neighbor Ir sites ( $\text{Ir}_{II}$ ). This in turn leads to the formation of two-dimensional metallic Rh-Ir<sub>II</sub> planes intercalated by unperturbed insulating Ir<sub>I</sub> planes. The emergence of this metallic state is assisted by the smaller SOC strength on the Rh site: The DOS indicates that the Rh  $t_{2g}$  states are located at more negative binding energies than the corresponding Ir states mostly due to smaller relativistic effects. As a consequence, since the upper Hubbard Rh-Ir- $t_{2g}$  states are located below the Fermi level, the lower Hubbard band loses electrons and becomes partially occupied. Upon Rh doping the canted AF-I state undergoes a substantial modification, manifested by the flipping of the net in-plane FM moment in the Rh-Ir<sub>II</sub> planes and lifts the magnetic ordering from the AF-I to the AF-II type. All our results are generally in reasonable agreement with available ARPES and neutron measurements.

#### ACKNOWLEDGMENTS

This work was supported by the China Scholarship Council (CSC)-Austrian Science Fund (FWF) Scholarship Program, by the joint FWF and Indian Department of Science and Technology (DST) Project INDOX (Project No. I1490-N19), and by the FWF-SFB ViCoM (Grant No. F41). Computing time at the Vienna Scientific Cluster was greatly acknowledged.

- 
- [1] B. J. Kim, H. Jin, S. Moon, J. Y. Kim, B. G. Park, C. Leem, J. Yu, T. Noh, C. Kim, S. J. Oh *et al.*, *Phys. Rev. Lett.* **101**, 076402 (2008).
  - [2] B. J. Kim, H. Ohsumi, T. Komesu, S. Sakai, T. Morita, H. Takagi, and T. Arima, *Science* **323**, 1329 (2009).
  - [3] G. Jackeli and G. Khaliullin, *Phys. Rev. Lett.* **102**, 017205 (2009).
  - [4] J. W. Kim, Y. Choi, J. Kim, J. F. Mitchell, G. Jackeli, M. Daghofer, J. van den Brink, G. Khaliullin, and B. J. Kim, *Phys. Rev. Lett.* **109**, 037204 (2012).
  - [5] J. Kim, M. Daghofer, A. H. Said, T. Gog, J. van den Brink, G. Khaliullin, and B. J. Kim, *Nat. Commun.* **5**, 4453 (2014).
  - [6] P. Liu, S. Khmelevskyi, B. Kim, M. Marsman, D. Li, X.-Q. Chen, D. D. Sarma, G. Kresse, and C. Franchini, *Phys. Rev. B* **92**, 054428 (2015).
  - [7] Y. Hou, H. Xiang, and X. Gong, *New J. Phys.* **18**, 043007 (2016).
  - [8] J. Kim, D. Casa, M. H. Upton, T. Gog, Y.-J. Kim, J. F. Mitchell, M. van Veenendaal, M. Daghofer, J. van den Brink, G. Khaliullin *et al.*, *Phys. Rev. Lett.* **108**, 177003 (2012).



- [9] S. Fujiyama, H. Ohsumi, T. Komesu, J. Matsuno, B. J. Kim, M. Takata, T. Arima, and H. Takagi, *Phys. Rev. Lett.* **108**, 247212 (2012).
- [10] F. Wang and T. Senthil, *Phys. Rev. Lett.* **106**, 136402 (2011).
- [11] H. Watanabe, T. Shirakawa, and S. Yunoki, *Phys. Rev. Lett.* **110**, 027002 (2013).
- [12] Y. K. Kim, O. Krupin, J. D. Denlinger, A. Bostwick, E. Rotenberg, Q. Zhao, J. F. Mitchell, J. W. Allen, and B. J. Kim, *Science* **345**, 187 (2014).
- [13] Y. J. Yan, M. Q. Ren, H. C. Xu, B. P. Xie, R. Tao, H. Y. Choi, N. Lee, Y. J. Choi, T. Zhang, and D. L. Feng, *Phys. Rev. X* **5**, 041018 (2015).
- [14] Y. K. Kim, N. H. Sung, J. D. Denlinger, and B. J. Kim, *Nat. Phys.* **12**, 37 (2015).
- [15] A. de la Torre, S. M. Walker, F. Y. Bruno, S. Ricc , Z. Wang, I. G. Lezama, G. Scheerer, G. Girit, D. Jaccard, C. Berthod *et al.*, *Phys. Rev. Lett.* **115**, 176402 (2015).
- [16] P. A. Lee, N. Nagaosa, and X.-G. Wen, *Rev. Mod. Phys.* **78**, 17 (2006).
- [17] Y. Klein and I. Terasaki, *J. Phys.: Condens. Matter* **20**, 295201 (2008).
- [18] M. Ge, T. F. Qi, O. B. Korneta, D. E. De Long, P. Schlottmann, W. P. Crummett, and G. Cao, *Phys. Rev. B* **84**, 100402(R) (2011).
- [19] J. S. Lee, Y. Krockenberger, K. S. Takahashi, M. Kawasaki, and Y. Tokura, *Phys. Rev. B* **85**, 035101 (2012).
- [20] T. F. Qi, O. B. Korneta, L. Li, K. Butrouna, V. S. Cao, X. Wan, P. Schlottmann, R. K. Kaul, and G. Cao, *Phys. Rev. B* **86**, 125105 (2012).
- [21] Y. Cao, Q. Wang, J. A. Waugh, T. J. Reber, H. Li, X. Zhou, S. Parham, N. C. Plumb, E. Rotenberg, A. Bostwick *et al.*, *Nat. Commun.* **7**, 11367 (2016).
- [22] J. P. Clancy, A. Lupascu, H. Gretarsson, Z. Islam, Y. F. Hu, D. Casa, C. S. Nelson, S. C. LaMarra, G. Cao, and Y.-J. Kim, *Phys. Rev. B* **89**, 054409 (2014).
- [23] F. Ye, X. Wang, C. Hoffmann, J. Wang, S. Chi, M. Matsuda, B. C. Chakoumakos, J. A. Fernandez-Baca, and G. Cao, *Phys. Rev. B* **92**, 201112(R) (2015).
- [24] X. Chen, T. Hogan, D. Walkup, W. Zhou, M. Pokharel, M. Yao, W. Tian, T. Z. Ward, Y. Zhao, D. Parshall *et al.*, *Phys. Rev. B* **92**, 075125 (2015).
- [25] V. Brouet, J. Mansart, L. Perfetti, C. Piovera, I. Vobornik, P. L. F vre, F. Bertran, S. C. Riggs, M. C. Shapiro, P. Giraldo-Gallo *et al.*, *Phys. Rev. B* **92**, 081117 (2015).
- [26] S. Calder, J. W. Kim, G. X. Cao, C. Cantoni, A. F. May, H. B. Cao, A. A. Aczel, M. Matsuda, Y. Choi, D. Haskel *et al.*, *Phys. Rev. B* **92**, 165128 (2015).
- [27] V. Popescu and A. Zunger, *Phys. Rev. Lett.* **104**, 236403 (2010).
- [28] V. Popescu and A. Zunger, *Phys. Rev. B* **85**, 085201 (2012).
- [29] C. Eckhardt, K. Hummer, and G. Kresse, *Phys. Rev. B* **89**, 165201 (2014).
- [30] M. Reticcioli, G. Profeta, C. Franchini, and A. Continenza, *J. Phys.: Conf. Ser.* **689**, 012027 (2016).
- [31] P. E. Bl chl, *Phys. Rev. B* **50**, 17953 (1994).
- [32] G. Kresse and J. Hafner, *Phys. Rev. B* **47**, 558 (1993).
- [33] G. Kresse and J. Furthm ller, *Phys. Rev. B* **54**, 11169 (1996).
- [34] J. P. Perdew, K. Burke, and M. Ernzerhof, *Phys. Rev. Lett.* **77**, 3865 (1996).
- [35] C. Martins, M. Aichhorn, L. Vaugier, and S. Biermann, *Phys. Rev. Lett.* **107**, 266404 (2011).
- [36] M. Kaltak, Ph.D. thesis, University of Vienna, 2015.
- [37] A. A. Mostofi, J. R. Yates, G. Pizzi, Y.-S. Lee, I. Souza, D. Vanderbilt, and N. Marzari, *Comput. Phys. Commun.* **185**, 2309 (2014).
- [38] C. Franchini, R. Kov  ik, M. Marsman, S. S. Murthy, J. He, C. Ederer, and G. Kresse, *J. Phys.: Condens. Matter* **24**, 235602 (2012).
- [39] M. K. Crawford, M. A. Subramanian, R. L. Harlow, J. A. Fernandez-Baca, Z. R. Wang, and D. C. Johnston, *Phys. Rev. B* **49**, 9198 (1994).
- [40] K.-H. Ahn, K.-W. Lee, and J. Kune , *J. Phys.: Condens. Matter* **27**, 085602 (2015).
- [41] M. A. Subramanian, M. K. Crawford, R. L. Harlow, T. Ami, J. A. Fernandez-Baca, Z. R. Wang, and D. C. Johnston, *Physica C* **235**, 743 (1994).
- [42] R. S. Perry, F. Baumberger, L. Balicas, N. Kikugawa, N. J. Ingle, A. Rost, J. F. Mercure, Y. Maeno, Z. X. Shen, and A. P. Mackenzie, *New J. Phys.* **8**, 175 (2006).
- [43] S. J. Moon, M. W. Kim, K. W. Kim, Y. S. Lee, J.-Y. Kim, J.-H. Park, B. J. Kim, S.-J. Oh, S. Nakatsuji, Y. Maeno *et al.*, *Phys. Rev. B* **74**, 113104 (2006).
- [44] M. Itoh, T. Shimura, Y. Inaguma, and Y. J. Morii, *Solid State Chem.* **118**, 206 (1995).
- [45] S. Chikara, D. Haskel, J.-H. Sim, H.-S. Kim, C.-C. Chen, G. Fabbri, L. S. I. Veiga, N. M. Souza-Neto, J. Terzic, K. Butrouna *et al.*, *Phys. Rev. B* **92**, 081114(R) (2015).
- [46] P. Liu, B. Kim, P. Kumari, P. Mahadevan, G. Kresse, D. Sarma, X.-Q. Chen, and C. Franchini (unpublished).